Applied Catalysis B: Environmental 152–153 (2014) 192–201

Contents lists available at ScienceDirect

Applied Catalysis B: Environmental

journal homepage: www.elsevier.com/locate/apcatb

Influence of nickel in the hydrogen production activity of TiO_2

E. Pulido Melián [a,*], M. Nereida Suárez [a,1], T. Jardiel [b], J.M. Doña Rodríguez [a,1], A.C. Caballero [b], J. Araña [a,1], D.G. Calatayud [b], O. González Díaz [a]

[a] Centro Instrumental Fisicoquímico para el desarrollo de Investigación Aplicada (CIDIA-FEAM), Departamento de Química, Universidad de Las Palmas de Gran Canaria, Edificio Polivalente I del Parque Científico Tecnológico, Campus de Tafira, 35017 Las Palmas de Gran Canaria, Spain
[b] Departmento de Electrocerámica, Instituto de Cerámica y Vidrio (CSIC), Kelsen, 5, 28049 Madrid,Spain

ARTICLE INFO

Article history:
Received 13 October 2013
Received in revised form 3 January 2014
Accepted 20 January 2014
Available online 27 January 2014

Keywords:
Hydrogen
Photocatalysis
Nickel
TiO_2

ABSTRACT

Sol–gel synthesised TiO_2 developed by our group was modified through the addition of nickel nitrate and ammonium carbonate in the synthesis process. Photocatalysts were synthesised with different Ni/Ti molar ratios (0.015, 0.030, 0.045) and constant Ni/N ratio equal to 1.5 and subjected to post-calcination at temperatures of between 400 °C and 700 °C. Characterisation was carried out with: X-ray diffraction (XRD), UV–vis diffusive reflectance spectroscopy (DRS), X-ray photoelectron spectroscopy (XPS), transmission electron microscopy-energy dispersive X-ray analysis (TEM-EDX), thermal analysis (TGA, DTA), aggregate size distribution, Fourier transform infrared spectroscopy (FTIR) and nitrogen adsorption-desorption isotherm (BET).

Photoactivity in terms of photocatalytic hydrogen production was tested using a suspension of photocatalyst at 25 vol.% methanol. With a continuous flow of N_2 in headspace the hydrogen produced was conducted to a gas chromatograph for quantification. No evidence of the presence of N was found in the photocatalyst. However, the presence of Ni enhanced TiO_2 photoactivity, with a calcination temperature of 550 °C resulting in the highest photoactivity value of 260.76 μmol h^{-1}.

© 2014 Elsevier B.V. All rights reserved.

1. Introduction

One consequence of the world's continued development and industrialisation is an ever-growing energy dependence. As fossil fuels continue to be the main energy source there is an urgent need to develop environmentally-friendly processes to obtain clean combustion energy or energy vectors as is the case of hydrogen with its high energy potential ($\Delta H^\circ = -285.71$ kJ mol^{-1}).

Photocatalytic hydrogen production is a promising field which allows the transformation of a renewable energy source, namely solar radiation, into chemical energy, in this case hydrogen.

The two fundamental photocatalytic hydrogen production methods are water photo-splitting and the photo-reforming of sugars/alcohols. The latter method is more advanced in terms of development with the presence of an easily oxidisable organic compound enhancing the efficiency of the electron-gap separation. In addition to the generation of an energy source, an added benefit of this method is the degradation of potentially contaminating waste materials.

As a result of its chemical stability, low cost and high photoactivity, one of the semiconductors which has attracted most interest is TiO_2 as shown by the extensive literature which cover its characterisation and application studies [1,2]. Many studies based on this semiconductor aim to modify it in order to obtain even better photocatalysts. Normally, these modifications consist of cation and anion doping [3–5] or are based on surface deposition. Traditionally, these deposits are comprised of noble metals such as Pt, Au and Ag, which have given very good results, or rare earths such as Ce or La [6], but the high costs involved restrict development at the application level of photocatalysis in general. For this reason, more and more studies aim to reduce costs by using other more common metals such as those corresponding to the transition metals, mostly in their oxide forms, like Ni or Cu [7–9]. These modifications principally try to impede e^-/h^+ recombination and enhance the band gap or photosensitizing to be photoactive in the visible range. A number of studies have been published in which more than one element has been added [10]. *p*-type and *n*-type oxide semiconductor composites appear to have important electrical and optical properties. Recent investigation has been carried out on the synergy of *p*-type and *n*-type semiconductors [11–13] which improves separation of photogenerated holes and electrons. NiO is one such possibility and, though some information is available in the literature principally concerning aqueous-phase organic compound degradation for which good results were obtained [14–18],

* Corresponding author. Tel.: +34 928457298; fax: +34 928457397.
E-mail addresses: elisendapm80@hotmail.com (E.P. Melián), ogonzalez@dqui.ulpgc.es (O.G. Díaz).
[1] Tel.: +34 928457298; fax: +34 928457397.

0926-3373/$ – see front matter © 2014 Elsevier B.V. All rights reserved.
http://dx.doi.org/10.1016/j.apcatb.2014.01.039

there is little to be found in relation to its application in hydrogen production.

In view of the above, modification was carried out in the present study of synthesised TiO_2 developed by our group which had resulted in a photocatalyst with significant photocatalytic activity, better even than P25, in terms not only of degradation of contaminants in aqueous suspension [19] but also in terms of hydrogen production [20]. This modification involved the addition of precursors of Ni and N in different ratios for the purpose of enhancing e^-/h^+ separation and narrowing the band gap. The resulting photocatalysts were extensively characterised using several techniques and their photocatalytic activity tested in hydrogen activity using methanol as sacrificial agent.

2. Materials and methods

BET surface area, pore volume and size were determined through N_2 adsorption at 77 K using a Micromeritics 2010 instrument.

Analyses of the crystalline structure were performed by X-ray diffraction (XRD Bruker D8 Advance) with a monochromatized source of Cu $K\alpha_1$ radiation (λ = 0.15406 nm) at 1.6 kW (40 kV, 40 mA); samples were prepared by placing a drop of a concentrated ethanol dispersion of particles onto a single crystal silicon plate. Crystal sizes in the different phases were estimated from line broadening of the corresponding X-ray diffraction peaks by using the Scherrer equation. Anatase–rutile fractions were calculated taking into account the relative diffraction peak intensities of crystalline planes (1 0 1) and (1 1 1) of anatase and rutile, respectively.

Diffuse reflectance spectra were recorded for all samples on a Varian Cary 5 spectrophotometer and the Kubelka–Munk function, $F(R_\infty)$, was applied to obtain the band gaps following the method proposed by Tandon and Gupta [21].

The high-resolution transmission electron microscopy (HRTEM) images and EDX analyses were obtained on a JEOL 2100F transmission electron microscope (TEM/STEM) operating at 200 kV and equipped with a field emission electron gun, providing a point resolution of 0.19 nm; samples were prepared by placing a drop of a dilute ethanol dispersion of nanoparticles onto a 300 mesh carbon-coated copper grid and evaporated immediately at 60 °C.

The infrared spectra of the samples in the range 4000–1000 cm^{-1} were recorded using a Nicolet iS10 spectrophotometer with DTGS detector (4 cm^{-1} resolution, 32 scans and mirror velocity of 0.6329 $cm\,s^{-1}$). The spectra were taken placing the samples between two CaF_2 windows.

Size distribution of aggregates in aqueous suspension was analysed using a Mastersizer Hydro 2000 SM unit.

Surface characterization by X-ray photoelectron spectroscopy (XPS) was conducted on a Leybold–Heraeus LHS-10 spectrometer equipped with an EA-200 MCD hemispherical electron analyser and a prechamber to remove chemisorbed water from their surfaces.

The concentration of Ni in the aqueous suspensions was measured by means of atomic absorption spectrophotometry (AAS) with a Varian AA 240Z with Zeeman background correction and electrothermal atomization in a graphite oven (GTA 120). Thermogravimetry-differential thermal analysis (TGA-DTA) was carried out simultaneously using a PerkinElmer PYRIS Diamond model. The analyses were performed using alumina crucibles for the reference and sample in an air atmosphere from ambient temperature to 1200 °C at a rate of 2 °C min^{-1}.

The photoreactor was a home-made design with 200 mL of aqueous suspension containing 25% methanol and a photocatalyst concentration of 1 g L^{-1}. The pH value of the aqueous suspension was set to 5 by means of the NaOH solution. The light source was a set of two Solarium Philips HB175 lamps, each equipped with four 15 W Philips CLEO florescent tubes. Emission spectrum was 300–400 nm with maximum peak at 365 nm. The photoreactor was operated in continuous mode by using N2 as inert dragging gas (10 mL min^{-1}) at 1 bar and room temperature. This nitrogen flow, controlled with mass-flow measurement systems, was used to displace the hydrogen produced by photo-splitting from the photoreactor headspace towards the GC measuring system. Hydrogen production was monitored for 8 h through analysis in a gas chromatograph (Varian 3600) equipped with an injection valve (VALCO type), a Molsieve 5A column and a TCD detector. Final mineralization degree and pH were measured with a Crison Basic20 pH-meter and a Shimadzu TOC-VCSN Total Organic Carbon analyser. Suspension concentrations of formaldehyde and formic acid were quantitatively measured by spectrophotometry [22,23].

2.1. Synthesis of photocatalysts

The synthesis carried out in this work was the same sol–gel method as described in reference [20] in which titanium butoxide (IV) was used as Ti precursor with the incorporation in aqueous phase of the precursors of Ni and N. Nickel nitrate ($Ni(NO_3)_2{\cdot}6H_2O$, Sigma–Aldrich 99.999%) and ammonium carbonate ($(NH_4)_2CO_3$, Fluka pure) were used, the same precursors as employed in reference [10]. The precursors were added to obtain 3 different Ni/Ti molar ratios, namely X1 (Ni/Ti = 0.015), X2 (Ni/Ti = 0.030) and X3 (Ni/Ti = 0.045), maintaining a constant Ni/N ratio equal to 1.5. These molar ratios were selected based on the results obtained by Zhang et al. for formaldehyde degradation [10]. They were subsequently subjected to calcination at temperatures of between 400 and 700 °C. The photocatalysts were named X1, X2 or X3 followed by the calcination temperature. The TNi-550 and TN-550 photocatalysts also refer to "X" series photocatalysts but with omission of the N or Ni precursor, respectively.

3. Results and discussion

3.1. XRD

Table 1 shows the results for crystal size of the TiO_2 anatase and rutile phases and the anatase phase percentage for the three series. It can be seen that evolution of crystal size is very similar. Additionally, the rutile phase appears for the three series at 600 °C, a value in concordance with the range of temperatures published in the bibliography for anatase-rutile phase transition [24] and only

Table 1
TiO_2 anatase and rutile crystal size and anatase percentage for the X1, X2 and X3 series.

	X1			X2			X3		
	Anatase/nm	Rutile/nm	%Anatase	Anatase/nm	Rutile/nm	%Anatase	Anatase/nm	Rutile/nm	%Anatase
400 °C	10.4	–	100	9.7	–	100	9.1		100
550 °C	26.1	–	100	26.1	–	100	24.7		100
600 °C	36.6	Traces	≈100	37.8	Traces	≈100	37.8	38.9	90.5
650 °C	47.5	64.6	87	47.1	64.32	77.4	52.4	70.7	52
700 °C	55.8	88.8	40.5	53.2	88.47	14	49.8	88.8	5.8

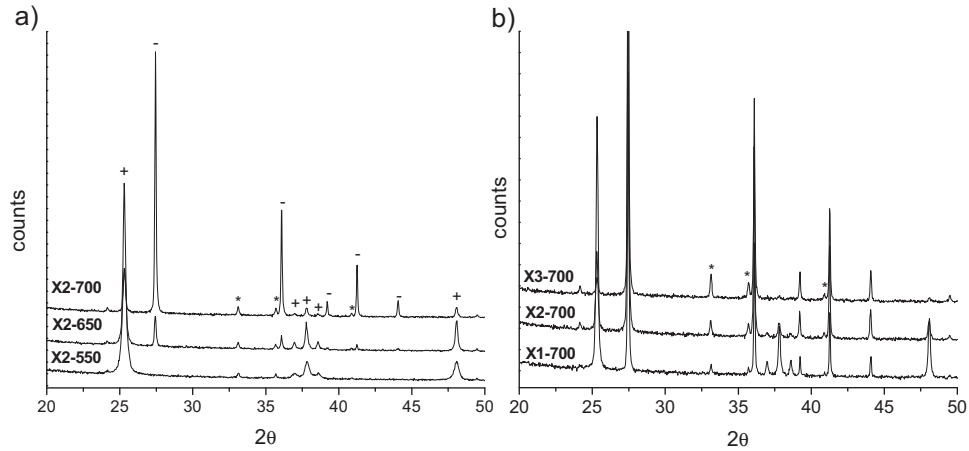

Fig. 1. XRD of (A) some selected samples of the X2 series and (B) comparison of the photocatalysts calcined at 700 °C of the three series. (+) Anatase, (−) rutile and (*) $NiTiO_3$.

slightly lower than the value recorded for synthesis without precursors [20]. Once the rutile phase appears it can be seen that the rutile:anatase ratio grows faster for the X3 series than for the X2 series which is in turn faster than for the X1 series. In the X3 series, 90.5% anatase at 600 °C changes to 5.8% for the X3-700, whereas for the X1-700 the corresponding value is 40.5% anatase. This rutilization effect is probably due to the Ni, as it has also been observed for other studies in which nickel acetylacetonate was used as Ni precursor [24]. However, what is notable here is how, despite a higher rutile percentage, there is no further increase in rutile crystal size with all three series obtaining a crystal size for 700 °C slightly below 89 nm.

However, anatase and rutile were not the only phases which appeared in these samples (Fig. 1). In addition, the $NiTiO_3$ phase (rhombohedral card JCPDS no. 33-0960) appeared at 600 °C for the X1 series and at 550 °C for the X2 and X3 series [25,26]. The diffraction peaks of $NiTiO_3$ are more intense for the X3 series, with higher Ni content. In each series this phase was more evident with the rise in calcination temperature. This is normal given that well crystallized $NiTiO_3$ requires high sintering temperatures of 600 °C [27]. This is in concordance with studies reported in the literature on the synthesis of Ni-Ti catalysts where $NiTiO_3$ has been observed at temperatures above 700 °C [28,29].

The peaks $2\theta = 36.4°$ and 41.2° of the NiO crystalline phase were not observed. However, the fact they were not detected does not necessarily mean they were not present. MacKenzie et al. [24] and M.A. Ahmed et al. [30] indicate in their studies with different Ni loads that the presence of NiO was not observed by XRD at concentrations below 5 mol%. So, the NiO may not have been found by XRD simply as a result of its low content and high dispersion [16].

3.2. BET surface area and pore size distribution

Table 2 shows the surface area and porosity results for the three photocatalyst series. It can be seen that the resulting solids from the synthesis have very high surface areas of between 374 and 470 $m^2\,g^{-1}$, with a reduction of between 60 and 74% when calcined at 400 °C and of around 90% at 550 °C.

Pore volume evolution is quite similar for the three series of samples. In all the series, as the calcination temperature increases pore volume falls and is lower than 0.1 $g\,cm^{-3}$ for temperatures above 550 °C.

The biggest difference between the three series is that the X3 series displays a more marked drop in surface area and pore volume compared to the other series at temperatures above 600 °C. This is in concordance with the more marked increase of rutile phase and crystal size in this series at temperatures above 600 °C, as seen in the XRD analyses. The higher Ni content in the synthesis process would seem to be the cause of these differences, leading to the greater formation of $NiTiO_3$ as the temperature rises to 700 °C at the expense of more dispersed forms such as NiO.

Fig. 2 shows the pore volume distribution for the three series. The most probable pore diameter in each series tends to increase with calcination temperature. The three series begin with a most probable pore diameter centred around 3.8 nm which, at 400 °C,

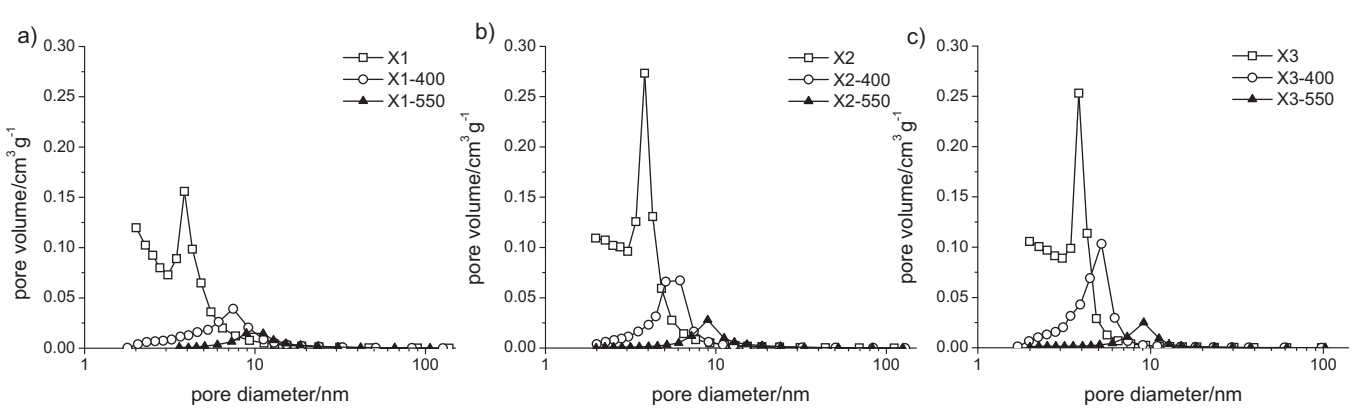

Fig. 2. Pore volume distribution for series (a) X1, (b) X2 and (c) X3.

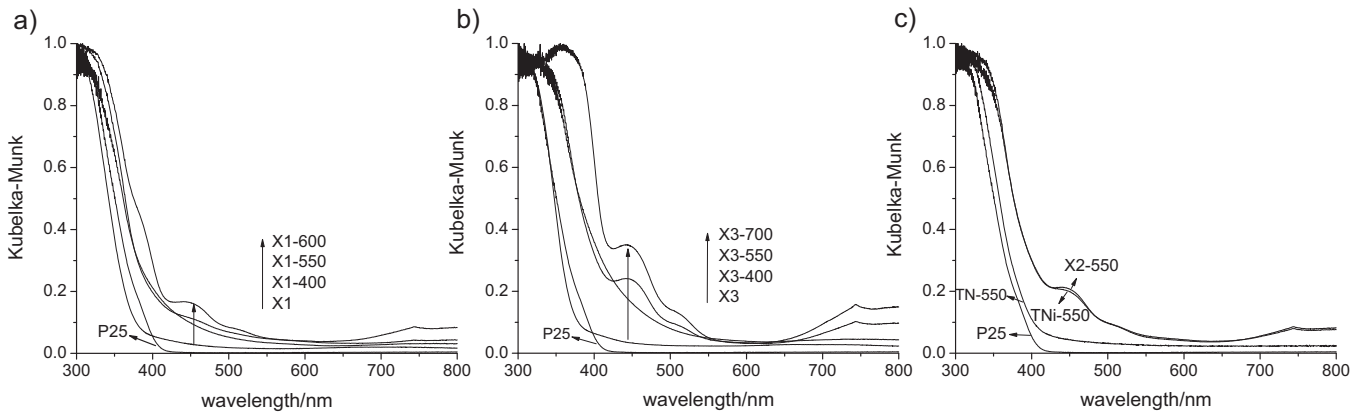

Fig. 3. Diffuse reflectance spectra of (a) series X1, (b) series X3 and (c) comparison of X2-550 with TNi-550 and TN-550. TiO_2 Aeroxide P25 (P25) is also shown for purposes of comparison.

Table 2
BET surface area and pore volume for the three photocatalyst series.

	X1		X2		X3	
	Surface/m²/g	Pore/cm³/g	Surface/m²/g	Pore/cm³/g	Surface/m²/g	Pore/cm³/g
Non-calcined	415.0	0.470	470.3	0.512	374.9	0.403
400	105.2	0.263	128.2	0.274	148.8	0.269
550	40.9	0.165	50.3	0.183	41.8	0.131
600	15.6	0.0751	26.3	0.124	17.9	0.0712
650	12.6	0.0741	13.9	0.0742	6.3	0.0379
700	2.9	0.0128	4.1	0.0269	1.5	0.0068

changes to 7.4 nm for X1, 6.2 nm for X2 and 5.2 nm for X3 and, at 550 °C, to approximately 9 nm for the three series. However, despite these similarities in the evolution of most probable pore diameter, it can be seen that the distributions are wider and more flattened for the X1 series compared to X2 and X3 which are similar in form.

3.3. Band gap and diffuse reflectance spectroscopy (DRS)

Fig. 3 shows the reflectance spectra, with those for P25 also included for purposes of comparison. In general, a significant shift can be seen of the band edge towards longer wavelengths when comparing the non-calcined sample (3.31 eV) and the photocatalyst calcined at 400 °C (3.01 eV for X1-400 and 2.85 for X2-400 and X3-400). These values are lower than the corresponding P25 band gap of 3.18 eV. No significant shift of the band gap is observed at higher temperatures though there is a notable increase of absorption in the visible range [31]. Additionally, in general, it can be observed that the Kubelka–Munk function does not become zero at high wavelengths for any sample of the three series, including the non-calcined samples. According to Fig. 2(c), which shows the reflectance spectra for the TNi-550 samples (sample without N precursor) and TN-550 (sample without Ni precursor), this absorbance at high wavelengths is due only to Ni and not to N.

The absorbances in the visible are even more significant as the calcination temperature rises in each series. An absorption band even appears around 500 nm at 550 °C. This band is more evident at this temperature for the series with higher concentration of precursors and, in general, increases with calcination temperature. It appears to be attributable to the $NiTiO_3$ phase as the appearance of the band coincides with the appearance of this crystalline phase [26].

3.4. Thermal analysis

Given the similarity that was apparent between the three series in terms of the shape of the curves from the TGA and DTA analyses, Fig. 4 only shows the analyses corresponding to the X2 series from 50 to 1200 °C. The TGA curves show two relevant regions in weight loss, from 50 to 180 °C and from 180 °C to about 400 °C. The first is due to dehydration and evaporation of organic substances which intervene in the synthesis. The second region with a significant weight loss corresponds to the burnout of hydroxyl groups and the organic substances. There was no obvious weight loss in the TGA curve above 400 °C. Total weight loss was 39.5%, 40.6% and 40.8% for the X1, X2 and X3 series, respectively.

The DTA curves present two clearly exothermic peaks in the region of highest weight loss due to decomposition of the organic compounds which participate in the synthesis, ethanol, citrates and carbonates. The first peak at about 215 °C is bigger than the second which is very near at 266 °C. No peak is observed at higher temperatures which might indicate endothermic decomposition of the

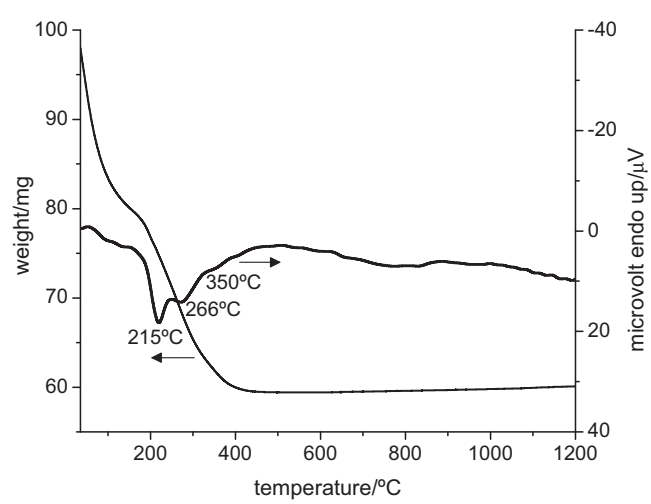

Fig. 4. TGA and DTA analysis for the X2 series.

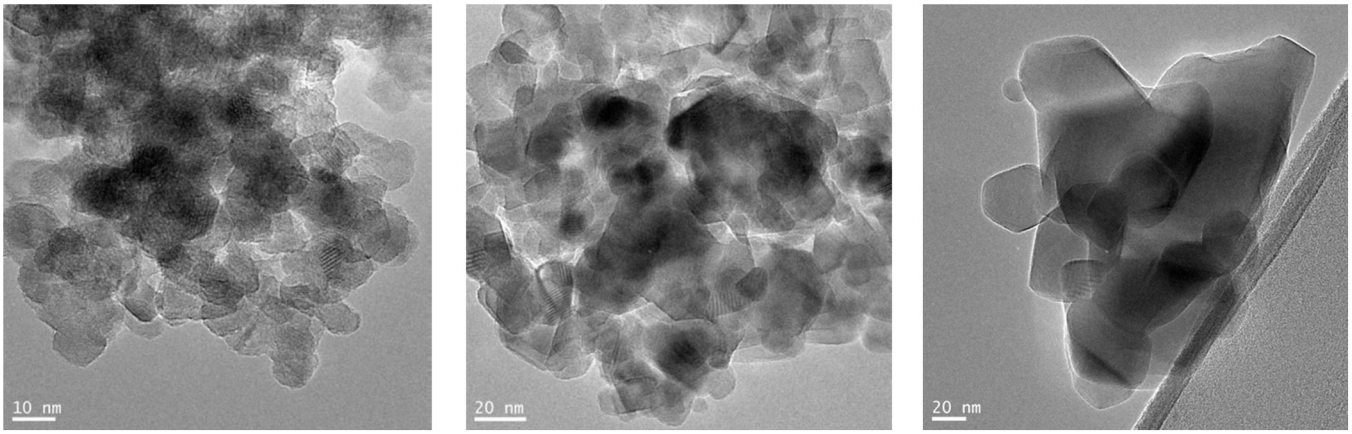

Fig. 5. HRTEM images of X2-400, X2-550 and X2-700.

nitrates or exothermic formation of NiO and $NiTiO_3$. There is only a slight indication around 350 °C of another small exothermic peak which may correspond to transformation of $NiNO_3$ to NiO [16,27], though the amount of NiO is so small that it is normal that it is practically indistinguishable in this study.

3.5. Transmission electron microscopy-energy dispersive X-ray analysis (TEM-EDX)

Fig. 5 shows the TEM micrographs of various selected samples from the X2 series: X2-400, X2-550 and X2-700. It can be seen how the particles are highly aggregated and how the size of the particles increases with calcination temperature showing significant size homogeneity at 700 °C.

EDX sampling (not shown) was performed for each of the above samples. The Ni signal for the X2-400 sample was more intense than for X2-550 and X2-700, indicating a higher concentration of Ni in the analyzed particles. The Ni/Ti ratios for the 4 analyzed areas of X2-400 were: 0.022, 0.028, 0.019 and 0.039. These results suggest a high degree of homogeneity in Ni distribution in the sample. This concurs with the fact that the NiO phase was not observed by XRD due to its high dispersion. Of the 8 analyses performed for X2-550, 3 areas were obtained in which Ni was not detected, 3 in which it was very difficult to quantify as the signal was in effect mixed up with the noise giving Ni/Ti values of around 0.006, and 2 areas in which Ni was abundant with Ni/Ti ratios of 0.012 and 0.013. Finally, Ni was not detected in 4 of the 5 sampled areas for X2-700, with a Ni/Ti ratio of 0.016 in the one area where it was detected.

From these analyses it can be deduced that as the calcination temperature increases Ni is more localized and not so dispersed in the bulk of the sample. This concurs with Ni forming the $NiTiO_3$ phase at higher temperatures, as shown by XRD.

It should also be mentioned that N was not detected by EDX in any of the samples analyzed.

3.6. Aggregate size distribution

Fig. 6(a) shows the aggregate size distribution for the X2 series. It can be seen that the distributions are practically unimodal. The most probable size for the non-calcined sample was 18.74 μm, gently shifting to lower values as the calcination temperature rose to 600 °C where the value was around 7 μm and then remaining steady for higher temperatures. Fig. 6(b) allows a comparison of the photocatalysts calcined at 550 °C in the three series. The distribution is wider for the X1 series and narrower for the X3 series. In addition, the distribution centre of the X1 series shifts to 29 μm compared to 12 μm for the X2 and X3 series. It should be remembered that the X1 porosity distribution was also different from the other two series.

It can be concluded from Figure 6(c) that the precursors of both Ni and N affect the photocatalyst aggregate size distribution. A bimodal distribution is even observed for TNi-550 with one peak centred around 20 μm of the same order as for the other photocatalysts, and another centred at a much higher value of 550 μm.

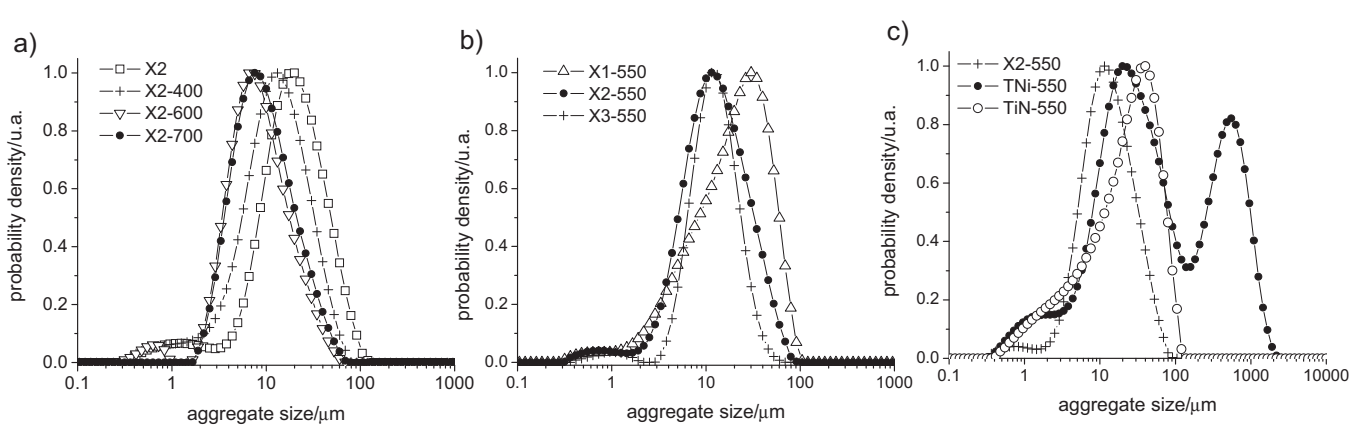

Fig. 6. (a) Aggregate size distribution for the X2 series. (b) Comparison at 550 °C of the three series. (c) Comparison of X2-550, TNi-550 and TN-550.

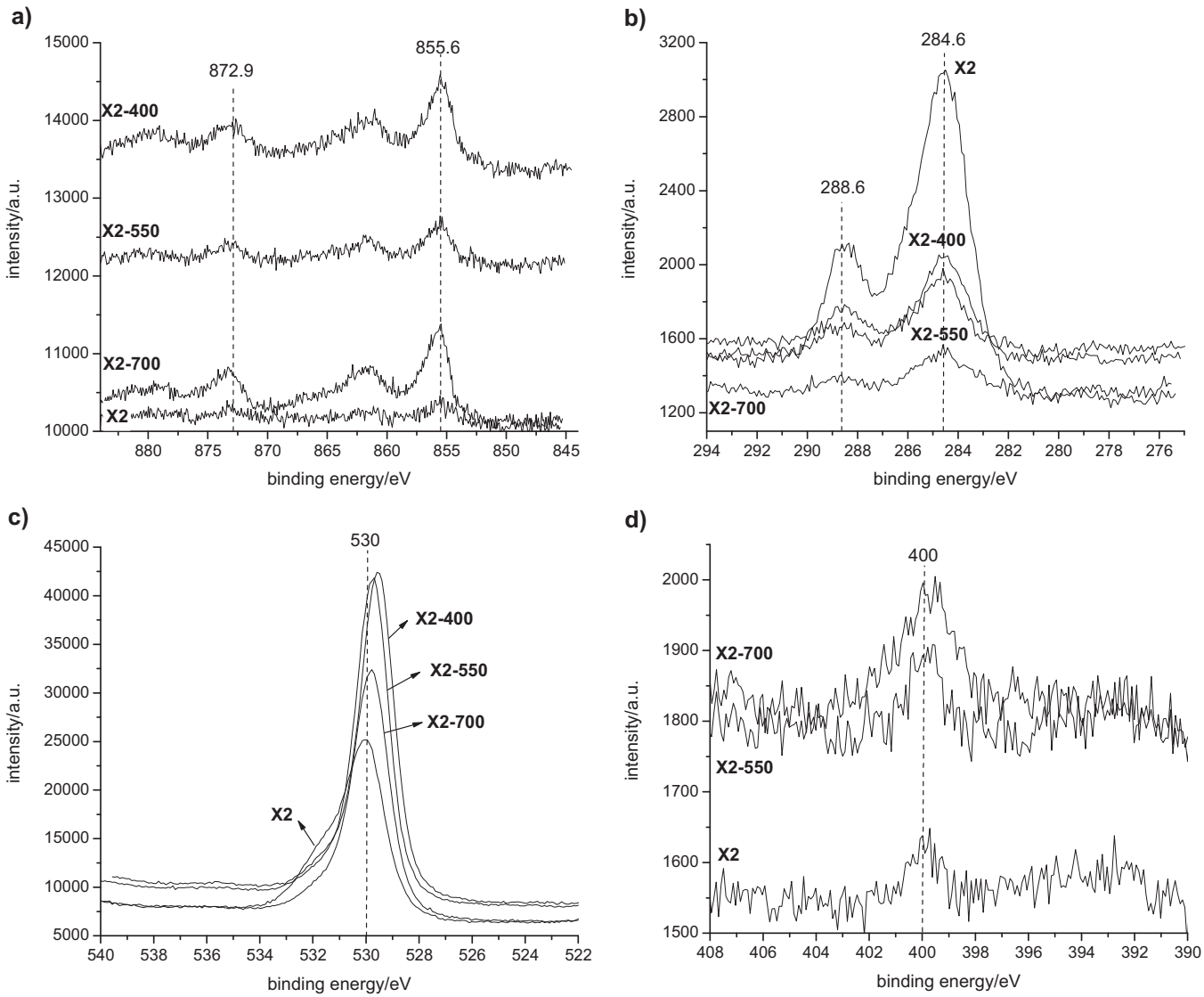

Fig. 7. XPS spectra for (a) Ni (2p) level, (b) C(1s) level, (c) O(1s) and (d) N(1s) level corresponding to X2 series.

3.7. X-ray photoelectron spectroscopy (XPS)

Table 3 and Fig. 7 show the results of the XPS analyses of selected samples of the X2 series.

Table 3
XPS results of the samples X2, X2-400, X2-550 and X2-700.

	X2		X2-400	
	Position/eV	at.%	Position/eV	at.%
Ti 2p	458.5	24.03	458.2	31.76
Ni 2p	855.6	0.52	855.6	1.4
O 1s	530.0	55.2	529.6	61.99
C 1s	284.6	19.05	284.6	4.31
N 1s	399.8	1.21	400.0	0.53
	X2-550		X2-700	
	Position/eV	at.%	Position/eV	at.%
Ti 2p	458.9	32.88	458.5	30.79
Ni 2p	855.5	0.79	855.8	1.89
O 1s	529.8	61.64	529.8	63.18
C 1s	284.6	4.11	284.6	3.67
N 1s	400.0	0.58	400.0	0.46

The binding energies of Ti(2p) and O(1s) are found at 458.5 eV and 529.8 eV, respectively, values which concur with those found in the bibliography for TiO_2 [32] and with an O/Ti ratio around 2. For the O (1s) peak, an additional small shoulder located at lower binding energies for X2 and X2-400 denotes the presence of surface OH groups (not shown).

Significant percentages of C and N can be seen in the non-calcined X2 sample. These are due to the precursors used for the synthesis. It can be seen with X2-400 that with the effect of calcination temperature these percentages are considerably reduced. At higher temperatures, the subsequent reduction is practically negligible concurring with the TGA analysis in which it was seen how weight loss occurred below 400 °C.

The amounts of nitrogen in the post-calcined samples are very low (around 0.5 at.%) and could even be attributable to atmospheric contamination. In any case, the position of N(1s) peak around 400 eV indicates that the nature of the nitrogen present on the surface corresponds to nitrogen impurities coming from nitrate, ammonium or atmospheric nitrogen but not to structural nitrogen since the binding energy of Ti–N corresponds to 396 eV [33]. So, as discussed in Section 3.3, the changes in the absorption spectrum with the calcination temperature are due to the Ni species.

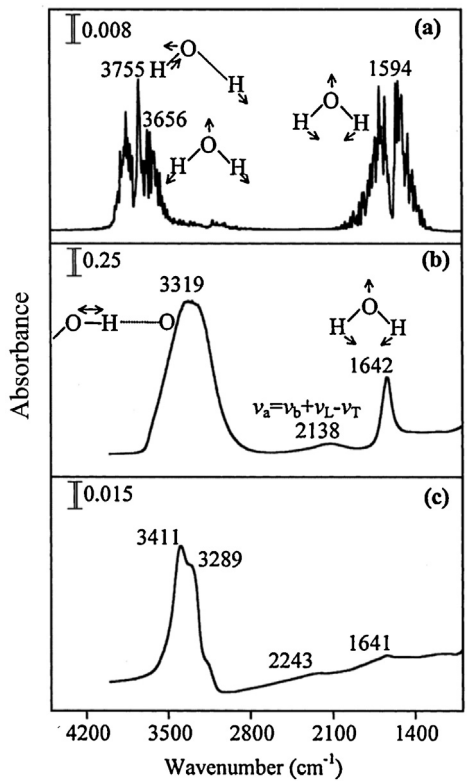

Fig. 8. FTIR spectra of water in gas (a), liquid (b) and solid (c) phase. Extracted from reference [32].

As for Ni, an increase is observed in the atomic percentage between X2 and X2-400 which is the result of elimination of the shadowing effect due to carbonaceous and nitrogenated species on the surface which is much cleaner at 400 °C. At 550 °C it falls again before increasing at 700 °C. This disappearance and appearance of Ni on the surface may be attributable to structural changes due to the appearance of the $NiTiO_3$ phase which the sample undergoes as the temperature rises and as shown by XRD and EDX.

An analysis of the X2-550 sample after the photocatalytic test (results not shown) also revealed no Ni^0. This suggests that though the reduction takes place during the photocatalytic test, subsequent contact with the air must have oxidized it [7].

3.8. Fourier transform infrared spectroscopy (FTIR)

According to some authors [34–36], the existence of adsorbed water on the semiconductor surface is necessary for photocatalytic activity to be sustainable. The idea is that the catalyst uses its surface water to generate the •OH radicals, which is the species considered directly responsible for attacking the organic matter.

Fig. 8 shows the water spectra in gas, liquid and solid phase taken from reference [37]. The band around 1640 cm^{-1} is attributed to the bending vibration (δH_2O) and the band centred at 3400 cm^{-1} is attributed to asymmetrical and symmetrical stretching vibrations (νOH) of the water. In solid state, where there are more bonds through hydrogen bridges, the band attributed to the (δH_2O) vibration is barely perceptible. In liquid state, where there is a lower number of bonds through hydrogen bridges, this vibration is more enabled and is observed with a relative intensity almost three times lower than that corresponding to the (νOH) vibrations. In gas phase both are of the same intensity.

Fig. 9 shows the FTIR of the X1-550, X2-550 and X3-550 photocatalysts which, as will be seen in section 3.9, gave the highest hydrogen production, and of the TNi-550 and TN-550 photocatalysts for comparison purposes. In the case of the photocatalysts which contain nickel, the relative intensity of the band at 1640 cm^{-1} is similar to the corresponding (νOH). This would suggest an interaction of the water in which the (δH_2O) vibration is equally benefitted as the (νOH) as occurs in the water spectrum in gas phase (Fig. 7). This type of interaction of the water with the photocatalyst is a weak one, allowing the hydrogen production reaction to take place without major hindrance. In Fig. 8(a), a proposal of this type of interaction is given.

Fig. 8(b) shows the TN-550 spectrum which is very similar to that of liquid water since the band at 1640 cm^{-1} is much lower than the band corresponding to the (νOH) vibrations. This type of interaction is stronger and a proposal for it is shown in Fig. 8(b). This photocatalyst was the lowest in terms of hydrogen production and we believe there may be a relationship between the mode of interaction of the water with the photocatalyst surface and the level of photoactivity. However, further research is required into this question.

It should also be mentioned that no bands were observed related to methanol nor to its degradation intermediates in the FTIR at the end of the photocatalytic runs.

Table 4
Concentration of leached Ni.

Photocatalyst	[Ni]/ppm	Photocatalyst	[Ni]/ppm
X2-400	6.0	X2-650	0.33
X2-550	1.9	X2-700	0.44
X2-600	0.56		

3.9. Photoactivity

Fig. 10(a) shows hydrogen production for the photocatalysts of the three series subjected to different calcination temperatures. The values shown in the figure correspond to the mean production rate in the final hour (see patterns in Fig. 10(b). The three series can be seen to follow the same trend. From 400 °C to 550 °C production rises and it is at this latter temperature that maximum production is achieved. From this point, production falls progressively as temperature rises. For all temperatures, the production sequence is X2 > X1 > X3. In short, the maximum production obtained for these photocatalysts of 260.72 μmol h^{-1} corresponds to the X2-550.

These changes in the pattern of hydrogen production vs. temperature (Fig. 10(a)) are closely related to the structural changes that the photocatalysts undergo. Between 400 °C and 550 °C the production rate rises as the crystallinity of the photocatalyst is enhanced. However, at temperatures above 550 °C we find that BET surface area and pore volume are extensively reduced. It is also at temperatures above 550 °C that $NiTiO_3$ and the rutile phase appear. In previous studies by our group it was observed that a low rutile phase percentage has a positive effect on hydrogen production [20]. Based on the above, the fall in hydrogen production above 550 °C would not appear to be due to the appearance of the rutile phase, bearing in mind that at 600 °C the percentage of anatase phase was at almost 100% for all the photocatalyst series.

Table 4 shows the concentration of leached Ni for the X2 series after conclusion of the photocatalytic tests and attaining equilibrium in darkness. It can be observed that as the calcination temperature rises leaching falls. This concurs with the structural observations that were made because, for the photocatalysts calcined at higher temperatures, the Ni is retained to a greater extent as it forms part of the crystalline structure of $NiTiO_3$ as observed by XRD.

So, the formation of $NiTiO_3$ not only appears to accelerate (i) the fall in BET surface area and pore volume and (ii) the increase in crystal size, as previously discussed when comparing the three

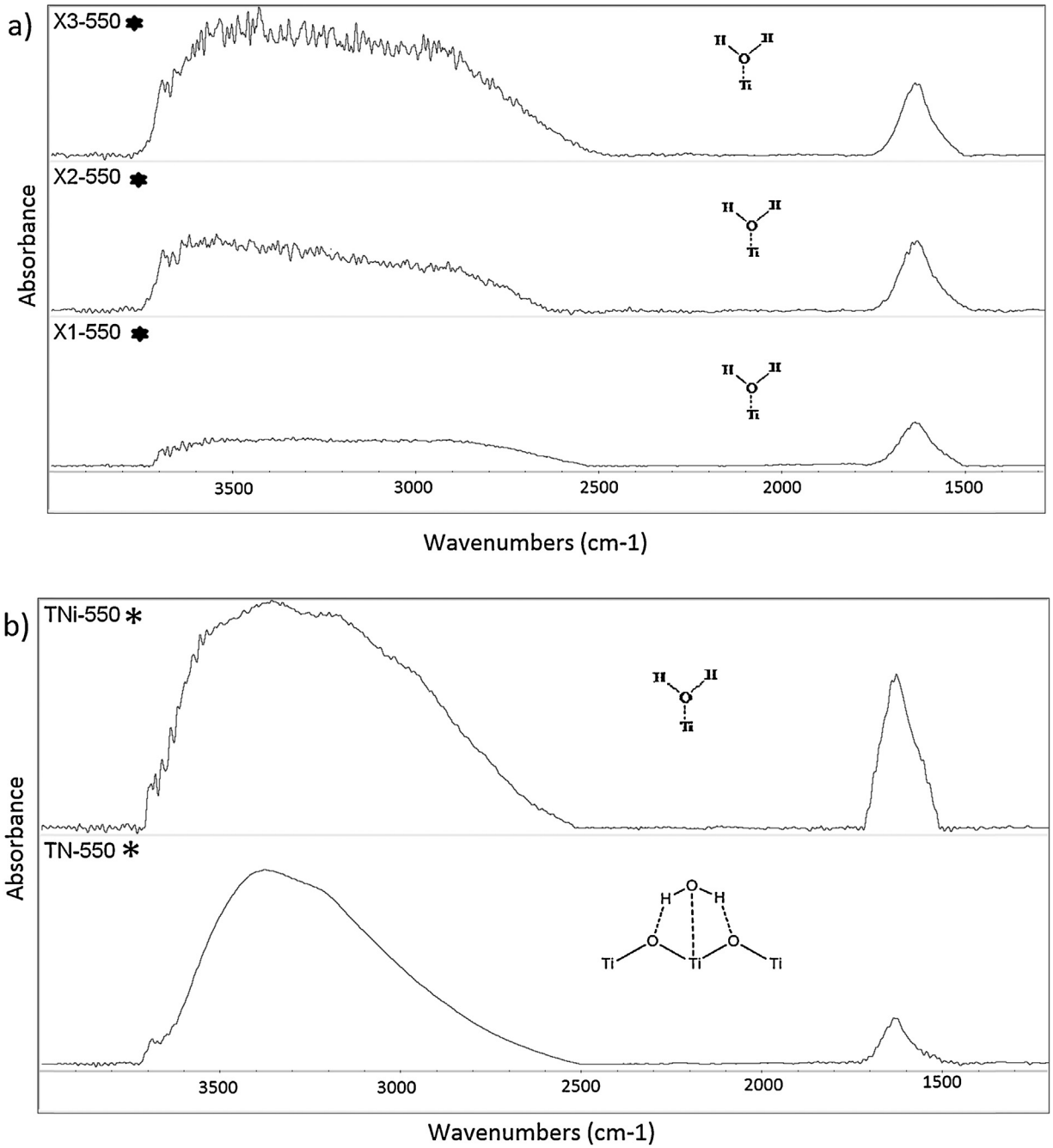

Fig. 9. (a) FTIR spectra of the photocatalysts X1-550*, X2-550* and X3-550*. (b) FTIR spectra of the photocatalysts TNi-550* and TN-550* (* indicates sample at end of the photocatalytic run and dried at room temperature for 72 h).

series of photocatalysts, but also to lower the homogeneity of Ni distribution on the photocatalyst surface and its ability to pass into solution, as observed in the XPS, EDX and leaching analyses.

The form in which the nickel is found in the photocatalyst appears to be a determining factor in its effect on photoactivity. Oxidized nickel as NiO homogenously distributed on the photocatalyst surface or available in solution to be adsorbed are suitable forms for the nickel to act as an electron trap and for its photoreduction [38,39]. According to Wang et al. [38], the activity of the Evonik P25 photocatalyst in hydrogen production is favoured by the presence of nickel dissolved in methanol, with nickel ions adsorbed on the photocatalyst surface photoreduced by the action of the light.

The species NiO and Ni^{2+}(aq) are more common in these photocatalytic systems before the formation of $NiTiO_3$. The incorporation of nickel in a more complex and stable structure as $NiTiO_3$ reduces its presence on the surface and its hunger for electrons.

Our group is presently working on the impregnation with nickel of pure TiO_2 synthesized with the same sol–gel process as used for the present work. Though we only have preliminary results, it would appear that surface impregnation of nickel is much more effective than its incorporation in the sol–gel synthesis process. It may be that its incorporation in the synthesis process leads to the formation during the thermal treatment of $NiTiO_3$, with a consequent negative effect on photoactivity.

The consequent fall in activity from 550 °C to 700 °C is due to the combined action of various factors: the lower surface area, the decrease in pore volume, the growth and increase in $NiTiO_3$

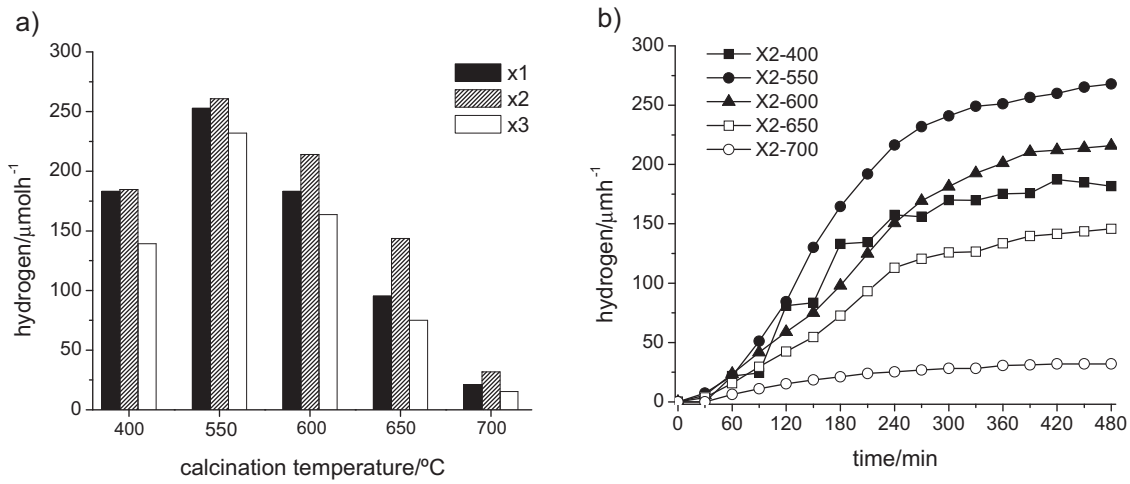

Fig. 10. (a) Hydrogen production in the three series of photocatalysts. (b) Pattern of hydrogen production for the X2 series.

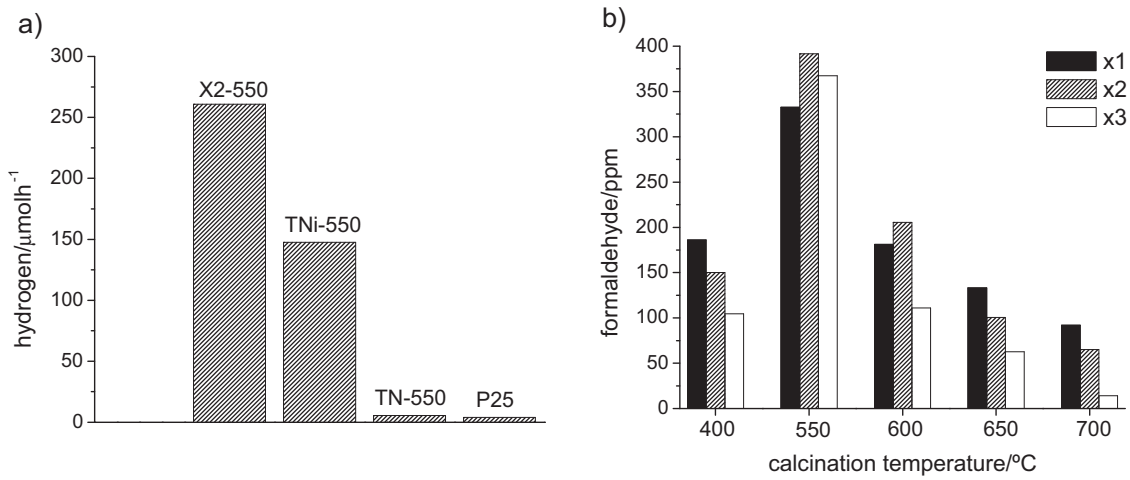

Fig. 11. (a) Hydrogen production of X2-550, TNi-550 and TN-550 (Evonik P25 has been added for comparison purposes). (b) Concentration of formaldehyde for the three photocatalyst series.

crystallinity observable by XRD, the decrease in Ni^{2+}(aq) and NiO and the extensive formation of rutile phase.

It can be observed in Fig. 11(a) that there is higher hydrogen production with the X2-550 compared to the TNi-550 or the TN-550. This may be due to the synergy of the two precursors, Ni and N. Since N, unlike Ni, was not incorporated in the structure of the photocatalysts, it appears to be simply that the incorporation of ammonium carbonate in the synthesis process has a positive effect on the final photoactivity of the photocatalyst. It has been reported in the literature [40] that ammonium carbonate increases surface area and porosity of the materials used. This appears to be the situation in our case, in that in the absence of ammonium carbonate there is a fall in surface area and pore volume from the respective values of 50.3 $m^2\,g^{-1}$ and 0.183 $cm^3\,g^{-1}$ for X2-550 to 34.4 $m^2\,g^{-1}$ and 0.0906 $cm^3\,g^{-1}$ for TNi-550. However, further research on this question is required.

The intermediates of methanol reported in the bibliography are formaldehyde and formic acid. It can be seen in Fig. 11(b) that the concentration of formaldehyde follows the trend of hydrogen production, with a maximum at 550 °C which for the X2 series corresponds to a concentration of 391 ppm. It was not possible to quantify the formic acid as its concentration was below the lowest detection limit of 0.1 ppm of the analytical techniques employed. In addition, no significant variation was observed with respect to the initial pH. Mineralisation was also not observed due to the high load of sacrificial agent, 25 vol.%.

4. Conclusions

In this work, highly active synthesized TiO_2 was modified with the incorporation in the synthesis process of precursors of Ni and N at three Ni/Ti molar ratios (0.015, 0.030, 0.045) and maintaining a constant Ni/N ratio equal to 1.5. These syntheses were calcined at temperatures ranging between 400 and 700 °C. The structural evolution of the three series of samples was very similar, though an increase in the rate of rutile formation was observed for the X3 series. Unlike Ni, N was not incorporated in the crystalline structure. At low calcination temperatures, Ni was highly dispersed in the photocatalyst forming NiO. As the calcination temperature increased Ni was more localized in the structure forming the $NiTiO_3$ phase. In addition, less Ni leached as calcination temperature rose. The appearance of the $NiTiO_3$ phase coincided with a fall in activity of these photocatalysts in the three series of samples. Maximum

hydrogen production of 260.76 μmol h^{-1} was obtained for X2-550, and no formic acid in solution was detected.

Acknowledgements

We are grateful for the funding of the Spanish Ministry of Science and Innovation and Spanish Ministry of Economy and Competitiveness for their financial support through the Project GESHTOS (IPT-120000-2010-033) and the Infrastructure Project UNLP10-3E-726, co-financed with FEDER funds.

References

[1] X. Cheng, S.S. Mao, Chem. Rev. 107 (2007) 2891–2959.
[2] A.D. Paola, G. Cufalo, M. Addamo, M. Bellardita, R. Campostrini, M. Ischia, R. Ceccato, L. Palmisano, Colloids Surf. A: Physicochem. Eng. Asp. 317 (2008) 366–376.
[3] S.U.M. Khan, M. Al-Shahry, W.B. Ingler Jr., Science 297 (2002) 2243–2245.
[4] T. Ohno, M. Akiyoshi, T. Umebayashi, K. Asai, T. Mitsui, M. Matsumura, Appl. Catal. A: Gen. 265 (2004) 115–121.
[5] R. Asahi, T. Morikawa, T. Ohwaki, K. Aoki, Y. Tage, Science 293 (2001) 269–271.
[6] J. Lin, J.C. Yu, J. Photochem. Photobiol. A: Chem. 116 (1998) 63–67.
[7] J. Yu, Y. Hai, B. Cheng, J. Phys. Chem. C 115 (2011) 4953–4958.
[8] W. Choi, A. Termin, M.R. Hoffmann, J. Phys. Chem. 98 (1994) 13669–13679.
[9] J. Bandara, C.P.K. Udawatta, C.S.K. Rajapakse, Photochem. Photobiol. Sci. 4 (2005) 857–861.
[10] X. Zhang, Q. Liu, Appl. Surf. Sci. 254 (2008) 4780–4785.
[11] J. Zhang, S.Z. Qiao, L. Qi, J. Yu, Phys. Chem. Chem. Phys. 15 (2013) 12088–12094.
[12] M. Miyauchi, Y. Nukui, D. Atarashi, E. Sakai, ACS Appl. Mater. Interfaces, Article ASAP doi:10.1021/am402929d Publication Date (Web): September 3, 2013.
[13] J. Cao, B. Xu, H. Lin, S. Chen, Chem. Eng. J. 228 (2013) 482–488.
[14] C.-S. Chou, Y.-J. Lin, R.-Y. Yang, K.-H. Liu, Adv. Powder Technol. 22 (2011) 31–42.
[15] G.G. Nakhate, V.S. Nikam, K.G. Kanade, S. Arbuj, B.B. Kale, J.O. Baeg, Mater. Chem. Phys. 124 (2010) 976–981.
[16] Y. Ku, C.-N. Lin, W.-M. Hou, J. Mol. Catal. A: Chem. 349 (2011) 20–27.
[17] S.H. Woo, W.W. Kim, S.J. Kim, C.K. Rhee, Mater. Sci. Eng. A 449–451 (2007) 1151–1154.
[18] L.G. Devi, N. Kottam, B.N. Murthy, S.G. Kumar, J. Mol. Catal. A: Chem. 328 (2010) 44–52.
[19] E.I. Seck, J.M. Doña Rodríguez, C. Fernández Rodríguez, D. Portillo Carrizo, M.J. Hernández Rodríguez, O. González Díaz, J. Pérez Peña, Sol. Energy 87 (2013) 150–157.
[20] E. Pulido Melián, O. González Díaz, A. Ortega Méndez, C. Rodríguez López, M.N. Suárez, J.M. Doña Rodríguez, J.A. Navío, D. Fernández Hevia, J. Pérez Peña, Int. J. Hydrog. Energy 38 (2013) 2144–2155.
[21] S.P. Tandon, J.P. Gupta, Phys. Status Solidi 38 (1970) 363–367.
[22] E.R. Kennedy, in: NIOSH Manual of Analytical Method (NMAM), Formaldehyde: Method 3500, 4th ed. Atlanta, 1994, Issue 2, pp. 2-5.
[23] K.H. Schaller, G. Triebig, in: H.U. Bergmeyer (Ed.), Methods of Enzymatic Analysis, VCH Publishers, Cambridge, UK, 1988, pp. 668–672.
[24] K.J.D. MacKenzie, Trans. J. Br. Ceram. Soc. 74 (1975) 29–34.
[25] Y.J. Lin, Y.H. Chang, W.D. Yang, B.S. Tsai, J. Non-Cryst. Sol. 352 (2006) 789–794.
[26] G.W. Zhou, Y.S. Kang, J. Disp. Sci. Technol. 27 (2006) 727–730.
[27] K.P. Lopes, L.S. Cavalcante, A.Z. Simoes, J.A. Varela, E. Longo, E.R. Leite, J. Alloy. Compd. 468 (2009) 327–332.
[28] H. Sun, J. Huang, H. Wang, J. Zhang, Ind. Eng. Chem. Res. 46 (2007) 4444–4450.
[29] A.B. Gambhire, M.K. Lande, S.B. Kalokhe, A.B. Mandale, K.R. Patil, R.S. Gholap, B.R. Arbad, Phil. Mag. Lett. 88 (2008) 467–472.
[30] M.A. Ahmed, J. Photochem. Photobiol. A: Chem. 238 (2012) 63–70.
[31] J. Yu, S. Wang, B. Cheng, Z. Lin, F. Huang, Catal. Sci. Technol. 3 (2013) 1782–1789.
[32] G. Colón, M.C. Hidalgo, G. Munuera, I. Ferino, M.G. Cutrufello, J.A. Navío, Appl. Catal. B: Environ. 63 (2006) 45–59.
[33] X. Chen, Y. Lou, A.C.S. Samia, C. Burda, L. Gole, Adv. Funct. Mater. 15 (2005) 41–49.
[34] H.S. Jung, J.-K. Lee, M. Nastasi, J.-R. Kim, S.-W. Lee, J.Y. Kim, J.-S. Park, K.S. Hong, H. Shin, Appl. Phys. Lett. 88 (2006) 013107-1–013107-3.
[35] L. Palmisano, M. Schiavello, A. Sclafani, G. Martra, E. Borello, S. Coluccia, Appl. Catal. B: Environ. 3 (1994) 117–132.
[36] P. Du, A. Bueno-López, M. Verbaas, A.R. Almeida, M. Makkee, J.A. Moulijn, G. Mul, J. Catal. 260 (2008) 75–80.
[37] H. Al-Abadleh, V. Grassian, Langmuir 19 (2003) 341–347.
[38] W. Wang, S. Liu, L. Nie, B. Cheng, J. Yu, Phys. Chem. Chem. Phys. 15 (2013) 12033–12039.
[39] J. Yu, J. Ran, Environ. Sci. 4 (2011) 1364–1371.
[40] T. Klimova, Y. Huerta, M.L.R. Cervantes, R.R.M. Aranda, J. Ramírez, in: G. Poncelat (Ed.), Preparation of Catalysts VI Scientific Bases for the Preparation of Heterogeneous Catalysts, Elsevier Science B.V., The Netherlands, 1995, pp. 411–420.